

# Experimental investigation of the performance of image registration and de-aliasing algorithms

Peter N. Crabtree, Phan D. Dao, and Richard H. Picard

*Air Force Research Laboratory, Space Vehicles Directorate  
29 Randolph Road, Hanscom AFB, USA*

## ABSTRACT

Various image de-aliasing techniques and algorithms have been developed to improve the resolution of sensor-aliased images captured with an undersampled point spread function. In the literature these types of algorithms are sometimes included under the broad umbrella of superresolution. However, in the current paper we consider them to be a form of image restoration, because we aim to restore image resolution lost due to sensor aliasing, but only up to the limit imposed by diffraction. Specifically, the work presented here is focused on image de-aliasing using microscanning. Much of the previous work in this area demonstrates improvement by using simulated imagery, or using imagery obtained where the subpixel shifts are unknown and must be estimated. This paper takes an experimental approach to investigate performance, in which the subpixel shifts are known *a priori* at some level. We use a CMOS camera, an ISO 12233 resolution target, and two linear translation stages which provide two-axis camera control via RS-232 interface. The translation stages provide a microstepping capability which allows discrete steps of approximately  $0.1 \mu\text{m}$ . The ISO 12233 target includes many features, including those for estimating the Line Spread Function and Modulation Transfer Function (MTF) via the tilted-edge response and Fourier transform, as well as square wave burst patterns for estimating the MTF more directly using the Contrast Transfer Function method. This target also includes a series of slightly tilted square wave burst patterns intended for measuring the aliasing ratio. We use one of these patterns to visually demonstrate successful de-aliasing.

## 1. INTRODUCTION

This paper presents results from our initial laboratory investigation of registration and de-aliasing algorithms applied to imagery from a visible sensor. For the work presented here we used a PixelINK PL-B741U camera based on a CMOS sensor. Section 2 provides necessary background on imaging theory, image registration and de-aliasing algorithms, resolution testing, and performance metrics. Methodology and approach are described in Sec. 3. Section 4 presents results based on imagery of an ISO 12233 resolution target collected with the CMOS camera. This includes results for object-space to image-space motion calibration, which is required because visual inspection only yields an estimate of object distance. A precise measurement is not straightforward when using a compound lens. Results for registration and de-aliasing algorithm performance are also presented. De-aliasing was accomplished in both the spatial and spatial frequency domains. Concluding remarks are provided in Sec. 5, including plans and recommendations for future work.

## 2. BACKGROUND

### 2.1. Imaging Theory Fundamentals

This section presents a summary of the standard imaging theory based on linear systems and Fourier optics. First, recall that for coherent light the imaging system is linear in complex amplitude, whereas for incoherent light the system is linear in intensity. For the incoherent case, the impulse response is the squared modulus of the amplitude impulse response, and the incoherent image intensity is given by

$$i = |\tilde{h}|^2 \otimes |u_g|^2 = |\tilde{h}|^2 \otimes i_g \quad , \quad (1)$$

where  $\tilde{h}$  is the complex amplitude (coherent) impulse response, and  $u_g$  and  $i_g$  are the perfect-system geometric-optics predictions for the image field and intensity, respectively. The impulse response, or Point Spread Function (PSF), for the incoherent case is given by  $h = |\tilde{h}|^2$ . Equation 1 is now written as

$$i = h \otimes i_g \quad . \quad (2)$$

The spatial frequency spectrum of the incoherent image intensity is given by [1]

$$I = \mathcal{H}I_g \quad , \quad (3)$$

where  $\mathcal{H}$  is the Optical Transfer Function (OTF). Note that quantities in Eq. 3 are the Fourier transforms of their normalized counterparts (lower-case) from Eq. 2:  $i$ ,  $h$ , and  $i_g$  are normalized to unit volume before transforming to Fourier space. In general, the OTF is a complex function. The OTF modulus is termed the MTF, while the OTF phase is termed the Phase Transfer Function.

The system MTF can be represented as the multiplication of component transfer functions [2]:

$$MTF_{system} = MTF_{diffraction} \times MTF_{detector} \quad . \quad (4)$$

For the work presented here we assume no relative motion (during sensor integration) between the object and imaging system, and therefore we have ignored the contribution of motion-induced blur to the system MTF. We have also ignored contributions to the overall MTF from the electronics and signal processing subsequent to spatial sampling and prior to processing by de-aliasing algorithms.

The diffraction-limited OTF for a circular aperture with no central obscuration is given by [1]

$$\mathcal{H}_{diffraction}(f) = \begin{cases} (2/\pi) \left[ \arccos(f/f_c) - (f/f_c)\sqrt{1 - (f/f_c)^2} \right] & , \quad f \leq f_c \\ 0 & , \quad \text{otherwise} \end{cases} \quad , \quad (5)$$

where  $f = (f_x^2 + f_y^2)^{1/2}$  is the magnitude of the radial spatial frequency vector and  $f_c$  is the frequency cutoff for an incoherent imaging system given by

$$f_c = \frac{D}{\lambda z_i} \quad , \quad (6)$$

where  $D$  is aperture diameter,  $\lambda$  is (center) wavelength, and  $z_i$  is the distance from the exit pupil to the image plane. For an object at infinity, the incoherent frequency cutoff is given by

$$f_c = \frac{1}{\lambda F} \quad , \quad (7)$$

where  $F$  is the optical system focal ratio or  $f$ -number.

The transfer function describing the spatial frequency response of pixels with a rectangular active area is given by [3,4]

$$\mathcal{H}_{detector}(f_x, f_y) = \text{sinc}(d_x f_x) \text{sinc}(d_y f_y) \quad , \quad (8)$$

where  $d_x$  and  $d_y$  describe the physical dimensions of the photosensitive area within a pixel in the horizontal and vertical directions, respectively. The corresponding detector MTF is

$$MTF_{detector} = |\text{sinc}(d_x f_x)| |\text{sinc}(d_y f_y)| \quad . \quad (9)$$

Also note that for a pixelated sensor such as a CCD or CMOS, and the case of equal pixel pitch along both axes, the Nyquist spatial frequencies along the two axes are equal and given by

$$f_{xs} = f_{ys} = \frac{1}{2d_{cc}} \quad , \quad (10)$$

where  $d_{cc}$  is the pixel pitch (i.e., center-to-center spacing along the two axes).

The system MTF as predicted by Eqs. 5 and 9 is presented as a surface plot in Fig. 1(a). Additionally, a cross-section of the MTF along the  $f_x$ -axis is presented in Fig. 1(b), including component MTFs describing *diffraction* and the *detector* subsystem. The detector Nyquist frequency given by Eq. 10 is also plotted in Fig. 1(b) as a point of reference (vertical blue line). The plots shown in Fig. 1 were calculated using the following parameter values: center wavelength  $\lambda = 600$  nm, focal ratio  $F/4$ , areal fill factor = 40%, and pixel pitch  $d_{cc} = 6.7$   $\mu\text{m}$ . These values correspond to experiment hardware described in Sec. 3.

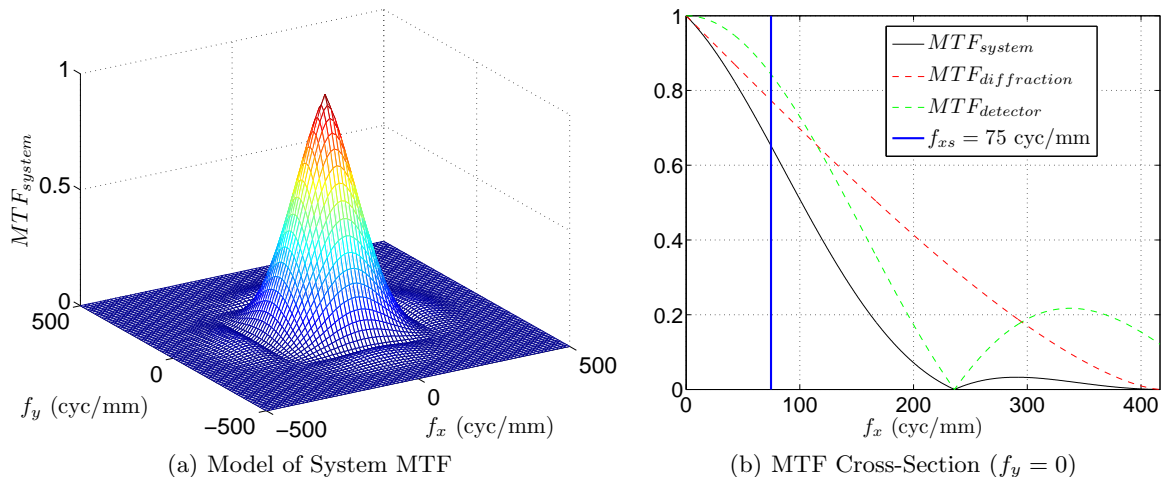


**Figure 1.** Analytic model of the system MTF plotted as a surface in (a) and as a cross-section along the  $f_x$ -axis in (b). The MTF was calculated using the following parameter values: center wavelength  $\lambda = 600$  nm, focal ratio  $F/4$ , areal fill factor = 40%, and pixel pitch  $d_{cc} = 6.7 \mu\text{m}$ . The component MTFs describing the contributions from *diffraction* and the *detector* are also plotted in (b), along with the sensor Nyquist spatial frequency  $f_{xs} = 75$  cyc/mm.

## 2.2. Image De-aliasing Algorithms

The goal of de-aliasing algorithms is to compensate for image degradation resulting from inadequate spatial sampling by the Focal Plane Array (FPA). Fig. 1(b) provides one illustration of this process; in this scenario the optical cutoff frequency (Eq. 7) is  $f_c = 417$  cyc/mm, which is 5.6 times the Nyquist frequency. Therefore, spatial frequencies greater than 75 cyc/mm and less than 417 cyc/mm are passed by the optical system, but aliased to lower frequencies when captured by the FPA. Our present goal is to mitigate the amount of aliased energy in the processed image.

To further illustrate the various sampling and signal processing regions, Fig. 2 presents two views of the relationship between the optical cutoff and sensor Nyquist frequencies. Fig. 2(a) plots the OTF cutoff (Eq. 7) as a function of focal ratio, as well as the Nyquist frequency (horizontal blue line). These two curves essentially divide the *spatial frequency–focal ratio* space into 3 regions of interest. First, the region below the horizontal blue line corresponds to spatial frequencies which are passed by the optics and properly sampled by the FPA. Second, frequencies above the blue curve and below the red curve are passed by the optics, but aliased due to inadequate spatial sampling by the FPA. Third, the area above the red curve describes spatial frequencies not passed by the optics due to diffraction. In other words, any useful frequency content in this region generated by post-processing algorithms is termed superresolution.

Next, Fig. 2(b) plots the ratio of the OTF cutoff frequency (Eq. 7) to the sensor Nyquist frequency (Eq. 10), as a function of focal ratio. This result highlights the fact that de-aliasing for a given wavelength range is only useful below a certain  $f$ -number. For this particular scenario,  $2d_{cc}/\lambda F > 1$  for  $F < 22.3$ . Also note that as pixel pitch is reduced there is a decreased potential for benefit from de-aliasing. However, one must also consider SNR and data bandwidth, which may drive a given design toward larger and/or fewer pixels. Therefore, even with ongoing improvements in sensor technology resulting in smaller pixels, there may still be applications and scenarios where de-aliasing will provide a valuable signal processing tool for improving image quality. Finally, note that for a focal ratio of  $F/4$ , the ratio plotted in Fig. 2(b) is equal to 5.6. In terms of our experimental setup, the aliasing ratio will be somewhat less than 5.6 due to factors such as optical aberrations and a finite object distance (see Eq. 6). Therefore, we chose 1/4 pixel for an initial microscanning step size.

The microscanning approaches described here basically use a sequence of frames recorded with known, or estimated, subpixel image shifts. In general the shifts are unknown, and a registration algorithm becomes a key component to successful de-aliasing. In terms of algorithm design, de-aliasing can be approached from both the image and spatial frequency domains. In the image domain the subpixel shifts are essentially used to directly generate a High Resolution (HR) grid. Although in some image-domain approaches, the HR image intensities are obtained by solving a constrained minimization problem [4]. On the other hand, the set of Low Resolution (LR) subpixel-shifted images can be transformed to spatial frequency space using the FFT, and then used to

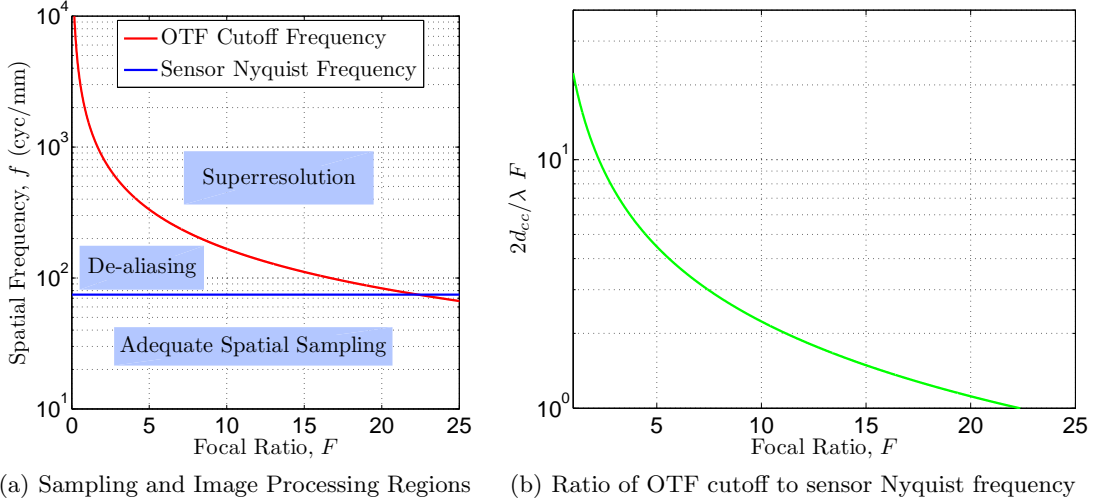


**Figure 2.** Two illustrations of the sampling and image processing regions of interest. Fig. (a) shows the OTF cutoff frequency (Eq. 7) as a function of focal ratio, as well as the Nyquist frequency (horizontal blue line). These values are based on a wavelength of  $\lambda = 600$  nm and a pixel pitch of  $d_{cc} = 6.7 \mu\text{m}$ . Fig. (b) shows the ratio of OTF cutoff frequency to the sensor Nyquist frequency, as a function of focal ratio.

form a system of linear equations (for each LR pixel). This set of linear systems can then be solved using linear algebra techniques to unscramble the aliased frequency content [5-7]. The inverse Fourier transform of this “unscrambled” spectrum yields the desired de-aliased image. This technique is described by the following equation:

$$\mathbf{y} = \Phi \mathbf{x} \quad , \quad (11)$$

where  $\mathbf{y}$  is a column vector of image DFT coefficients,  $\Phi$  is a matrix of complex exponential factors relating the DFT coefficients of the shifted images to coefficients of the aliased (i.e., overlapping) copies of the Continuous Fourier Transform (CFT), and  $\mathbf{x}$  is a column vector of unknown CFT coefficients. Values for  $\mathbf{y}$  are taken from the set of 2D FFTs of the image sequence, and the matrix  $\Phi$  is generated based on knowledge of the subpixel shifts and an assumed aliasing ratio. Note that Eq. 11 is solved for each point in the LR grid, and each solution yields a set of reconstructed CFT coefficients which are then placed in the HR FFT grid.

### 2.3. Image Registration Algorithms

A wide variety of image registration algorithms have been investigated and developed over the past several decades. Several algorithms were utilized during the course of this effort, to include:

- The basic phase correlation technique [8]
- The modified phase correlation technique for subpixel registration described by Foroosh, et al. [9]
- A subpixel registration technique described by Guizar-Sicairos, et al. [10] (MATLAB® code available on-line)

The first algorithm, the basic phase correlation technique, only provides a shift estimate to the nearest integer number of pixels. Therefore, this technique is not useful for de-aliasing, but does provide a foundation for the development of other algorithms. The following two algorithms do provide a subpixel shift estimate. For this work, we assume only a global image translation. The original image intensity is described by  $f(x, y)$ , and the shifted image is  $g(x, y) = f(x - x_0, y - y_0)$ . The phase correlation technique and its variations are based on the normalized cross power spectrum:

$$\frac{\mathcal{F}(f)\mathcal{F}(g)^*}{|\mathcal{F}(f)\mathcal{F}(g)^*|} = \exp\{2\pi j(f_x x_0 + f_y y_0)\} \quad . \quad (12)$$

After computing the normalized cross spectrum given by the left side of Eq. 12, the resulting (ideally) planar phase modulation is transformed back to the image domain via the inverse FFT. The location of the resulting

peak provides an estimate of the phase tilt, which corresponds to an estimate of the image shift. The approach of Foroosh [9] is based on a multi-rate signal processing formulation of the phase correlation technique. Essentially, this method involves fitting a Dirichlet function to the peak pixel and its neighbors. The simplified approach to this fitting as presented by Foroosh is very straightforward to implement; only a few additional lines of code are required once the basic phase correlation technique has been implemented. Finally, the approach of Guizar-Sicairos [10] is a very efficient implementation of Fourier interpolation, which is used to refine the estimate produced by the basic phase correlation technique.

## 2.4. Optical System Resolution Targets and Testing

A variety of techniques and standardized targets have been developed and utilized for testing the resolution of optical systems. Some of these, such as the USAF 1951 Target and the NBS 1952 Target, are based exclusively on a set of 3- or 4-bar patterns where each pattern is of a certain spatial frequency. This type of target can be used to infer the limiting spatial frequency by visual inspection, or to estimate the value of the MTF at several different spatial frequencies by way of the Contrast Transfer Function (CTF). Another approach to resolution testing is through the use of random test patterns. This idea is analogous to the use of a white noise pattern in acoustics to determine system frequency response, as well as the “FFT method” of generating atmospheric phase-screens [11] for wave-optics simulations. For this work we used the ISO 12233 target developed for high definition television (HDTV) applications [12]. The ISO 12233 target includes several slanted knife-edge targets for the purpose of computing the MTF by Fourier transform. They are offset from the vertical or horizontal by 5 degrees so that the edges will be sampled at many different phases, which allows estimation of the spatial frequency response beyond the Nyquist frequency of the sampling (equivalent to the moving knife edge approach).

## 2.5. Performance Metrics

Typical metrics used to characterize the resolution of an imaging system include:

- Optical Transfer Function [*SPATIAL FREQUENCY DOMAIN*]
  - Modulation Transfer Function
  - Phase Transfer Function
- Limiting Resolution (at a specified contrast) [*SPATIAL FREQUENCY DOMAIN*]
- Resolution [*IMAGE DOMAIN*]
  - Rayleigh
  - Sparrow

For some applications and object scenes of interest, the limiting resolution may not be the best metric for describing system performance. The shape of the MTF curve below or above the limiting resolution may be of greater importance. Ultimately, the spatial frequency content of the scene determines the importance of a system’s ability to resolve a particular spatial frequency.

# 3. METHODOLOGY AND APPROACH

## 3.1. Experiment Setup

A PixeLINK CMOS camera was used to investigate algorithm performance. Key specifications for this camera are provided in Tab. 1. An Edmund Optics Focusable 25 mm Double Gauss Lens (#NT55-326) was used with the PixeLINK camera. This lens has a minimum working distance of 240 mm, and a manually adjustable aperture allowing focal ratios of  $F/4$  to  $\infty$ . The design MTF for the lens is approximately equal to 0.1 at a spatial frequency of 300 cyc/mm. This is approximately 4 times the sensor Nyquist limit, which guides our choice of  $1/4$  pixel for the initial microscanning step size. Significant resolution improvement is not expected to result from microscan increments considerably smaller than  $1/4$  pixel, as diffraction becomes the limiting factor. An Edmund Optics Enhanced Digital Camera Resolution Chart (#NT58-940) was used as a test object. This chart complies with the ISO 12233 standard. To implement a microscanning capability for these experiments, two linear motion stages were combined to allow computerized  $x$ - $y$  motion control of the PixeLINK camera via RS-232 interface. More specifically, we used two Zaber Linear stages (KT-LS28-I) and a 90 degree angle bracket (AB90-I). According to the Zaber documentation, the distance per microstep is  $0.09921875 \mu\text{m}$ . A typical setup with the PixeLINK camera attached to the Zaber stages is shown in Fig. 3.

**Table 1.** Key specifications for the PixeLINK PL-B741U CMOS camera.

	<b>PixeLINK PL-B741U</b>
Spectral Response	visible (400-700 nm)
Resolution	1280x1024 pixels
Frame Rate	27 Hz (full frame)
Sensor Type	CMOS
Bit Depth	8 or 10
Pixel Pitch	6.7 $\mu\text{m}$
Fill Factor	40%
Interface	USB 2.0

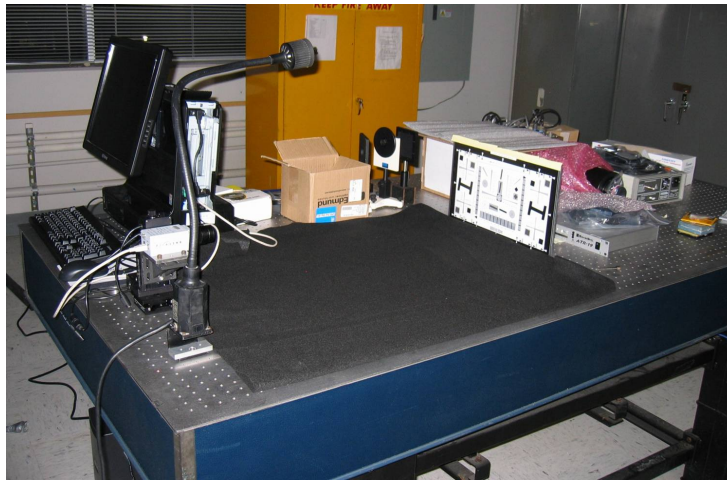


**Figure 3.** A typical experiment setup with the PixeLINK camera attached to two microstepping linear translation stages.

### 3.2. Data Collection Plan

Once the camera, linear motion stages, and ISO 12233 resolution target were installed, several data sets were taken sequentially to accomplish both actuator-to-image motion calibration, as well as registration and de-aliasing algorithm testing. Essentially, three distinct data sets were collected.

First, a series of images was collected using a set of linearly spaced positions spanning nearly the full range of actuator motion. This was accomplished first for shifts along the  $x$ -axis, then for shifts along the  $y$ -axis. Furthermore, this data was collected using both the *absolute* and *relative* command modes allowed by the control software interface to verify correct operation of the actuators. This data is used to calibrate the image de-magnification factor due to the fact that the object distance is only approximately known based on visual inspection. The object distance measurement is not straightforward when using a compound lens.

Second, a series of images was collected using a set of (roughly) log-spaced positions spanning nearly the full range of actuator motion. Again, separate data sets were collected for  $x$ - and  $y$ -axis motion. This data was only collected in the *absolute* actuator command mode. Given that there are greater than 280,000 available positions along each axis, log-spaced image positions were required to provide a useable amount of data while still utilizing the full range of motion. This data set is used to investigate the performance limits of the registration algorithms.

Finally, several sets of microscan data were collected for the purpose of demonstrating de-aliasing algorithm performance. The calibration factor resulting from analysis of the first data set was used to determine the number of microsteps per image shift prior to collecting the microscan data. First, 16 images were collected using  $1/4$  pixel shifts in  $x$  and  $y$ . Second, 36 images were collected using  $1/6$  pixel shifts. These two data sets then allow de-aliasing at  $1/2$ ,  $1/4$ ,  $1/3$ , and  $1/6$  subpixel shifts.

### 3.3. Calibration Procedure

A result of our experiment setup is that actuator motion occurs in object space. The observed image shift  $\Delta x_i$  (in pixels) is a linear function of the physical actuator shift  $\Delta x_o$  (in microsteps):

$$\Delta x_i = \frac{\beta}{d_{cc}} \left( \frac{f_L}{z_o - f_L} \right) \Delta x_o \quad , \quad (13)$$

where  $\beta$  is the physical distance per microstep (meters),  $d_{cc}$  is pixel pitch (meters),  $f_L$  is lens focal length (meters), and  $z_o$  is object distance (meters). Equation 13 is utilized twice during the calibration procedure. First, the object distance  $z_o$  is simply measured by visual inspection. An initial calibration factor is then calculated using the slope term of Eq. 13. This initial estimate is then used to adjust the number of microsteps per image shift as desired before collecting the set of linearly spaced calibration data as described in Sec. 3.2. Once collected, the calibration data is analyzed using one or more registration techniques, such as those described in Sec. 2.3. The shift between each image and the first image in the sequence is estimated. This yields a set of cumulative shift estimates (in image space) which are plotted as a function of the corresponding actuator displacement (in object space). The slope of a best-fit line,  $\hat{m}$ , to this data yields an estimate of the desired calibration factor. Conversely, this slope estimate can also be used to solve for an estimate of the object distance:

$$z_o = f_L \left( \frac{\beta}{d_{cc}\hat{m}} + 1 \right) \quad , \quad (14)$$

based on known parameters values from specifications for the camera, lens, and linear motion stages.

## 4. RESULTS

This section presents results for object-space to image-space motion calibration, as well as for performance of the registration and de-aliasing algorithms. All results presented herein are for an object distance of 34.5 in. (876.3 mm), as measured by visual inspection. Furthermore, all images were recorded as 8-bit monochrome bitmaps using the PixelINK OEM software. The lens aperture was wide open for a focal ratio of  $F/4$ .

### 4.1. Actuator-to-Image Motion Calibration

Once the linear motion stages, camera, and resolution target were installed on the optical table, the object distance was visually estimated to be  $z_o \approx 876.3$  mm. Using the slope term of Eq. 13, the corresponding calibration factor was found to be 2299.4 microsteps/pixel. This value was then used to choose 5174 microsteps per image shift, which equates to approximately 2.25 pixels per shift. This allowed collection of a maximum 54 images along each axis, as limited by the 28 mm range of the Zaber linear stages. The sequence of 54 images was then analyzed (using the three image registration algorithms described in Sec. 2.3) in order to estimate the shift between each image and the first image in the sequence. For the case of relative mode actuator displacement along the column direction only, the resulting set of estimates of the cumulative row- and column-direction shifts are plotted in Figs. 4(a) and 4(b), respectively, as a function of actuator displacement.

Application of linear regression to the data seen in Fig. 4(b) yielded slope estimates of  $422.7 \times 10^{-6}$ ,  $422.4 \times 10^{-6}$ , and  $422.5 \times 10^{-6}$  pixels per microstep for the basic phase correlation technique, the technique of Foroosh, and the technique of Guizar-Sicairos, respectively. For these three data sets, the residual fit error was least for the Guizar-Sicairos registration algorithm. Therefore, this was taken as the best calibration factor estimate. Using this slope estimate together with Eq. 14, the actual lens-to-object distance was also estimated to be 902 mm. The difference between this value and the original visual estimate is 2.5 cm, which is reasonable. Also note the results of Fig. 4(a), which show a slight upward trend in row ( $y$ -axis) position. This may be due to an imperfectly balanced load and/or a slight imperfection in one or both of the right-angle bracket attachments.

This same process was applied to calibration data for the three remaining cases: (1) absolute mode actuator displacement along column-direction, (2) relative mode actuator displacement along row-direction, and (3) absolute mode actuator displacement along row-direction. There was very little variation in the resulting calibration factor estimates, and for the remaining work presented in the paper the calibration was take as 2368 microsteps/pixel. This value was used to set the image shift values prior to recording the registration and de-aliasing data sets.

Alternatively, known dimensions of the ISO 12233 target can be used to estimate the calibration factor. Using one of the existing calibration images, the vertical size of the active resolution target area was estimated to be

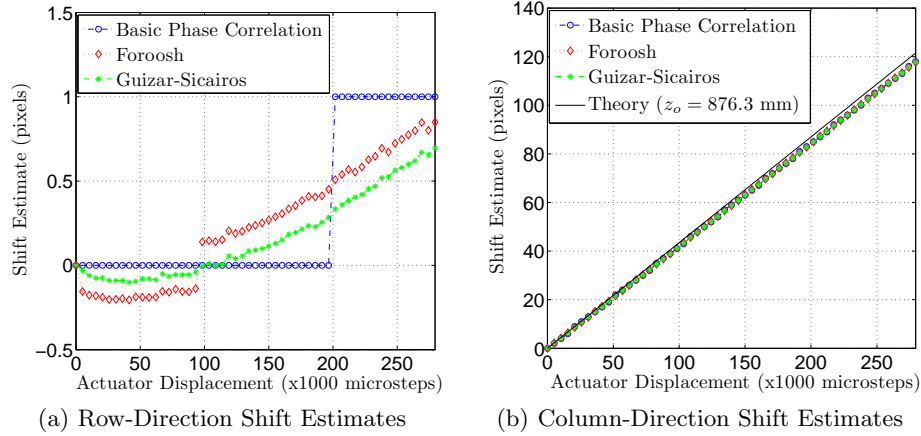


**Figure 4.** Estimates of global image shift (translation) for Relative Mode Actuator Displacement along column-direction ( $x$ -axis) only. Results for row- and column-direction shift estimates are presented in (a) and (b), respectively.

roughly 855.5 pixels. The actual object height is 200 mm, which together with the known physical distance per microstep gives 2356 microsteps per pixel. This is slightly smaller than the result of the linear regression approach. However, a more robust and systematic effort would require an automated process for estimating the image edge location in multiple images, then calculating an average. This effort was put off for the future since the linear regression method is robust and straightforward to implement.

#### 4.2. Registration Algorithm Performance

All three registration algorithms described in Sec. 2.3 were used to estimate the shift between each image and the first image in the sequence captured using log-spaced actuator positions. The magnitude of the resulting cumulative shift estimates are plotted versus the true (calibrated) shifts in Figs. 5(a) and 5(b) for  $x$ - and  $y$ -axis shifts, respectively. These results are plotted in log-log space to highlight the effective limit of the two subpixel registration algorithms considered. The technique of Foroosh [9] is unable to estimate shifts less than about 0.2 pixels. The technique of Guizar-Sicairos is able to estimate much finer shifts, but is more computationally expensive and requires more memory. The performance is controllable, to some extent, by choice of input parameter  $\alpha$ . However, running MATLAB<sup>®</sup> on a WinXP machine with 4 GB of memory resulted in an out of memory error when  $\alpha$  was increased to 5000. The parameter  $\alpha$  basically determines the extent of zero-padding used to perform the Fourier interpolation. Another aspect of registration algorithm failure not clearly identified by Figs. 5(a) and 5(b) is the inability to identify the correct sign of the shift. Based on our investigation to date,

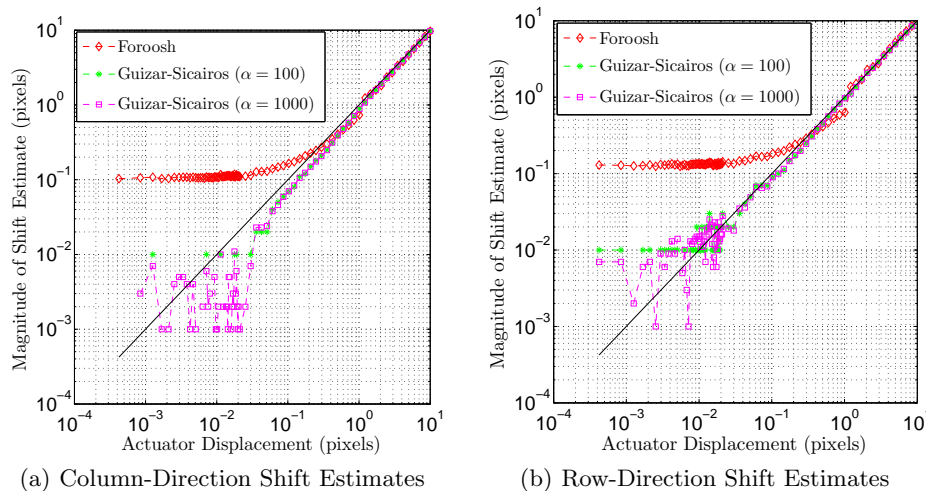


**Figure 5.** Estimates of cumulative global image shift (translation) for relative mode actuator displacement. Shift estimates along the column ( $x$ -axis) and row ( $y$ -axis) directions are presented in (a) and (b), respectively.

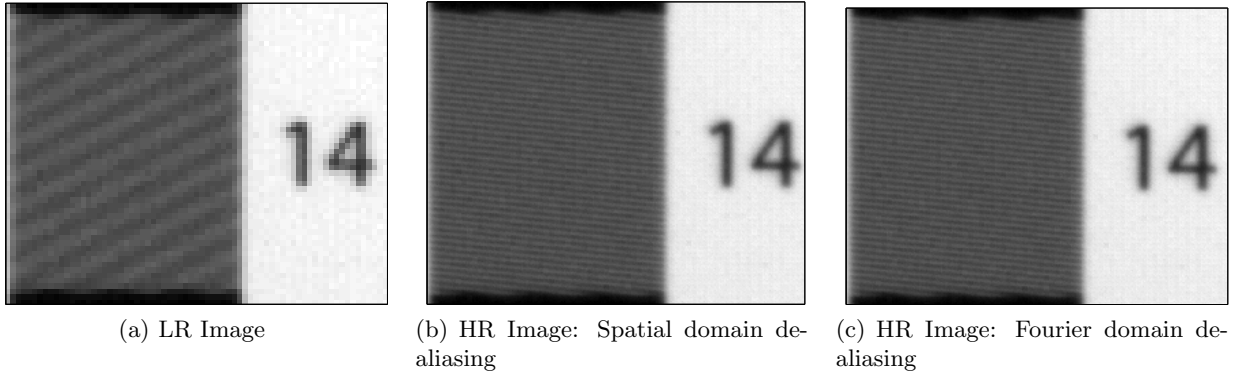


**Figure 6.** Example of image de-aliasing algorithm performance using 1/4 pixel microscan data. The original LR image is shown in (a), while (b) and (c) show the result of spatial and Fourier domain de-aliasing, respectively.

this sign flip is mainly a problem for the Foroosh algorithm, and becomes more prevalent as the shift becomes smaller. This could be a serious issue for a generalized de-aliasing algorithm relying solely on shift estimates as provided by a registration algorithm. In terms of the data collected for this work, this type of error could be related to the level of aliasing in the image data. One area worth more consideration is to extend the method of Foroosh by using a more robust procedure for fitting the Dirichlet function to the normalized cross spectrum image.

### 4.3. De-Aliasing Algorithm Performance

The calibrated 1/4 pixel shift microscan data set was processed using both the spatial and Fourier domain techniques. This resulted in a restored image of a large portion of the ISO 12233 target. To demonstrate the performance of these algorithms, Fig. 6 shows several versions of a closeup of one of the ISO 12233 slanted square wave burst (i.e., single spatial frequency) patterns. The image in Fig. 6(a) is from one of 16 LR images in the 1/4 pixel microscan sequence. The image in Fig. 6(b) is from the HR image produced using spatial domain processing. Due to the use of calibrated motion, the spatial domain technique was implemented as simple interlacing. The image in Fig. 6(c) is from the HR image produced using Fourier domain processing. In both HR images, the aliased spatial frequency apparent in the LR image has been removed. In this particular example, the spatial and Fourier domain techniques yield a result that is virtually identical based on visual inspection.

## 5. CONCLUSIONS

This paper describes a simple experimental setup to test the performance of image registration and de-aliasing algorithms. Once the calibration procedure is accomplished, the number of microsteps per pixel is known, and utilized to collect two additional data sets. The first is a set of images at log-spaced actuator positions to evaluate registration algorithm performance. The second is a set of microscan data covering a regular grid using a calibrated subpixel shift.

Using the log-spaced data we evaluated the basic phase correlation technique for global translation registration, as well as two variations thereof allowing subpixel shift estimation. The technique of Foroosh was simple to implement with little computational burden beyond that of the basic technique. However, for the data we collected this technique was unable to properly estimate shifts smaller than about 0.2 pixels. The technique of Guizar-Sicairos was evaluated using the authors' code (available on-line), and was able to estimate much smaller shifts to at least 1/100th of a pixel. This technique is more computationally intensive and requires more memory, but is somewhat adjustable by an input parameter controlling the amount of Fourier interpolation.

The microscan data was then processed using both the spatial and Fourier domain techniques. A visual example of the result of each technique was presented by way of an image of a slanted square wave burst pattern on the ISO 12233 resolution target. This example demonstrates that both techniques have successfully mitigated the aliasing evident in the LR image.

Thoughts and directions for future work include the following:

1. Explore the impact of the pixel fill factor

2. Extend the laboratory setup to include rotation and scale (i.e., target range)
3. Explore the impact of bit-depth by using the raw 10-bit PixeLINK image format (\*.pds)
4. Explore the impact of scene complexity, or level of “information” content, on algorithm performance
5. Investigate performance of the registration and de-aliasing algorithms in the Long-Wavelength Infrared (LWIR) using a microbolometer camera
6. Explore a more robust fitting procedure to extend the registration algorithm of Foroosh
7. Explore other registration techniques, such as those based on optimization to minimize a given error metric
8. Explore de-aliasing algorithm performance as a function of increasing noise and registration errors. Does this result depend on whether the registration errors are random or systematic?
9. How do registration errors compare with errors in the de-aliasing process itself in determining the fidelity of the de-aliased image?

Item number 4 above is related to potential application of de-aliasing to space-based imaging. One can imagine two scenarios: resolved and non-resolved. For the resolved case, one can reasonably expect that registration algorithm technology combined with relative motion between the object and camera will provide the necessary subpixel shifts, and measurements thereof, to implement de-aliasing. However, for the case of non-resolved sensing the registration algorithms may fail due to lack of scene content. There may be an algorithmic approach to address this issue. If not, additional hardware would be required that would allow the FPA to be actively scanned in subpixel increments in a deterministic fashion. This is related to vibration reduction technology used in some consumer digital cameras. Therefore, a straightforward technology path to this solution may already exist. Furthermore, the goal of de-aliasing in the resolved case is to improve the resolution and accuracy of an image. However, in the non-resolved case the probabilities of detection and false alarm are more appropriate metrics. This difference in performance metric deserves further study.

## REFERENCES

1. Goodman, J. W., *Introduction to Fourier Optics, 3rd ed.*, Roberts and Company, Englewood, CO (2005).
2. Holst, G. C. and Lomheim, T. S., *CMOS/CCD Sensors and Camera Systems*, JCD Publishing, Winter Park, FL (2007).
3. Hobbs, P. C. D., *Building Electro-Optical Systems – Making It All Work*, John Wiley & Sons, Inc., New York (2000).
4. Hardie, R. C., Barnard, K. J., Bognar, J. G., Armstrong, E. E., and Watson, E. A., “High-resolution image reconstruction from a sequence of rotated and translated frames and its application to an infrared imaging system,” *Opt. Eng.* **37**, 247–260 (January 1998).
5. Tsai, R. Y. and Huang, T. S., “Multipleframe image restoration and registration,” *Advances in Computer Vision and Image Processing, vol. 1*, 317–339 (1984).
6. Stevenson, R. L. and Borman, S., “Image sequence processing,” *Encyclopedia of Optical Engineering*, 840–879 (2003).
7. Park, S. C., Park, M. K., and Kang, M. G., “Super-resolution image reconstruction: A technical overview,” *IEEE Signal Processing Magazine*, 21–36 (May 2003).
8. Zitová, B. and Flusser, J., “Image registration methods: a survey,” *Image and Vision Computing* **21**, 977–1000 (2003).
9. Foroosh, H., Zerubia, J. B., and Berthod, M., “Extension of phase correlation to subpixel registration,” *Image Processing, IEEE Transactions on* **11**, 188–200 (March 2002).
10. Guizar-Sicairos, M., Thurman, S. T., and Fienup, J. R., “Efficient subpixel image registration algorithms,” *Optics Letters* **38**, 156–158 (January 2008).
11. McGlamery, B. L., “Computer simulation studies of compensation of turbulence degraded images,” *SPIE/OSA* **74**, 225–233 (1976).
12. ISO 12233:2000(E), *Photography – Electronic still-picture cameras – Resolution measurements*.